Gains and Losses in PbS Quantum Dot Solar Cells with Submicron Periodic Grating Structures

Yukihiro Hara,*[,†] Abay Gadisa,[‡] Yulan Fu,[†] Timothy Garvey,[†] Kristina T. Vrouwenvelder,[‡] Christopher W. Miller,[†] Jillian L. Dempsey,[‡] and Rene Lopez[†]

[†]Department of Physics and Astronomy and [‡]Department of Chemistry, University of North Carolina at Chapel Hill, Chapel Hill, North Carolina 27599, United States

ABSTRACT: Corrugated structures are integral to many types of photoelectronic devices, used essentially for the manipulation of optical energy inputs. Here, we have investigated the gains and losses incurred by this microscale geometrical change. We have employed nanostructured electrode gratings of 600 nm pitch in PbS colloidal quantum dot (PbS-CQD) solar cells and investigated their effect on photovoltaic properties. Solar cells employing grating structure achieved a 32% and 20% increase in short-circuit current density (J_{sc}) and power conversion efficiency, respectively, compared to nonstructured reference cells. The observed photocurrent increase of the structured devices mainly stems from the enhancement of photon absorption due to the trapping of optical energy by the grating structures. This optical absorption enhancement was particularly high in the near-infrared portion of the sun spectrum where PbS-based solar cells commonly present poor absorption. We have interestingly observed that the open-circuit voltage of all the devices increase with the increase in the absorbed photon energy (at a fixed light intensity), indicating a significant shift in Fermi energy level due to localization of low photon energy generated carriers in the tail of the density of states. We elucidate the role of the grating structure on charge dynamics and discuss the feasibility of these structures for construction of cheap and efficient photovoltaic devices.

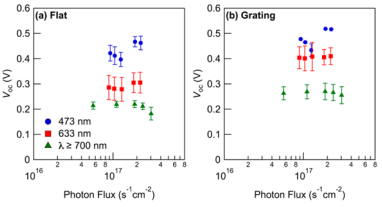

INTRODUCTION

PbS semiconducting colloidal quantum dots (CQDs) have been investigated in recent years in a growing number of electro-photonic devices such as solar cells,[1−4] light-emitting diodes,[5−7] photodetectors,[8] and other sensors.[9] This interest arises from the CQDs unique characteristics such as ease of bandgap tunability through control of particle size[10,11] and other convenient practical considerations such as low temperature solution processability. While the solution-based processing has created opportunities for printing films on substrates, the tunable energy bandgap has enabled fabrication of solar cells capable of harvesting a wide range of solar energy.[12−14] As a result, recent studies have demonstrated photovoltaic devices with remarkable short-circuit currents (J_{sc}) in excess of 20 mA/cm^2.[1−3,15] However, the majority of the photogenerated carries in PbS-based solar cells come from the high-energy photons (400−800 nm) whereas the external quantum efficiency (EQE) for near-infrared (NIR) photons is limited to less than 50%.[1−3,15] This marked difference in EQE results from the smaller penetration depth of shorter wavelength radiation, and therefore the majority of free charge carriers generated by these higher energy photons are closer to or within the depletion region allowing them to be effectively collected.[16] As typical PbS CQDs can absorb light well in the NIR range (800 nm to up to 1500 nm depending on particle size), it is critical to harvest these photon energies more efficiently to improve device performance.

Nanostructured electrodes offer great opportunities for enhancing both the optical energy absorption and carrier collection efficiency simultaneously. CQD solar cells are characterized by a narrow depletion width, which enforces electrically dead zones. Carriers produced in the dead zone cannot be collected at electrodes due to inherent short carrier transport lengths.[16] In nanostructured devices, however, the electrical field spatial distributions change substantially, thereby allowing for increased collection of charge carriers in addition to just pure optical absorption enhancement. Unique nanostructures such as nanowires,[17,18] nanopillars,[19] and other microstructures[20] have been suggested as a strategy to improve the cell performance. Kramer et al. have investigated a pillar structured electrode and demonstrated PbS-based solar cells with power conversion efficiency as high as 5.6%, exhibiting a 20% improvement in J_{sc} vs its flat counterpart.[19] Labele et al. have reported an efficiency of 9.2% for a device possessing a hierarchical structured electrode.[20] Performing full optoelectronic simulations, we have previously shown the benefits of introducing a simple grating structure in CQD solar cells, leading to further improvements in device power conversion efficiency.[21]

In this work we build upon our theoretical simulations by fabricating PbS CQD solar cells with a periodic submicron grating structure and experimentally investigate differences in electrical behavior compared to planar cells. The device with the grating structures showed ∼32% higher J_{sc} as well as 20%

Received: February 12, 2016
Revised: April 1, 2016
Published: April 13, 2016

higher power conversion efficiency compared to the flat reference device. Going beyond the optical differences between flat and patterned devices, we emphasized investigating the routes of electronic losses in device performance. This is accomplished by studying carrier recombination using light intensity dependent current−voltage measurements. Concurrently, the open-circuit voltage (V_{oc}) was found to be dependent on the wavelength of the incident light, whereby lower values were achieved when the devices were exposed to a near-infrared light. The wavelength dependent V_{oc} is attributed to the shift of Fermi level due to carrier localization in the tail of the density of states, a process that is highly dependent on the energy of the absorbed photons. The behavior of V_{oc} and fill factor (FF) will be discussed in detail. Overall, the results give complete information on the role of device engineering on performance, which substantially could help to redesign quantum-dot-based solar cells.

EXPERIMENTAL SECTION

Materials. Lead oxide (PbO(III), 99.999%), oleic acid (99%), 1-octadecene (ODE, 95.0%), hexamethyldisilathiane (TMS, synthesis grade), 3-mercaptopropionic acid (MPA, 99%), 1,3-benzenedithiol (BDT, 99%), anhydrous hexane (95%), and anhydrous acetonitrile were purchased from Sigma-Aldrich and used without further purification. Acetone, methanol, and hexane were purchased from Fisher Scientific. S1811 Positive photoresist, Thinner "P", and MF319 developer were purchased from Microchem.

Synthesis of PbS Colloidal Quantum Dots. PbS colloidal quantum dots (CQDs) were synthesized following the procedures published in the literature.[22,23] 0.45 g (2 mmol) of PbO(III) and 1.13 g (4 mmol) of oleic acid were dissolved in 17.7 mL of ODE and stirred at 100 °C under vacuum for over 1 h. The solution was then heated to 150 °C, and N_2 gas was flowed to the reaction flask. 0.21 mL (1 mmol) of TMS solution in 5.1 mL of ODE was prepared in another flask under N_2. The TMS solution was injected to PbO/oleic acid solution and stirred for 150 s followed by quenching in an ice bath. The PbS colloidal solution was then transferred to centrifuge tubes and precipitated in acetone. After centrifugation (7500 rpm, 10 min), the centrifuge-decant method was utilized to clean the PbS. In this method a small amount of hexane is used to resuspend the PbS, which is again precipitated in acetone and centrifuges. These steps were repeated three times, and then methanol was used in place of acetone for an additional two times. The oleic acid-capped PbS quantum dots were then dispersed in hexane for employment in the solar cell construction.

Fabrication of Grating Electrode. Commercial ITO (indium tin oxide) on glass was used as substrate in all the samples. Laser interference photolithography was then employed to create a submicron grating structure composed of a positive photoresist S1811, which was then to become a template for deposition of additional ITO and tantalum-doped TiO_2 (Ta:TiO_2). The photoresist was spin-coated at 7000 rpm for 40 s onto the commercial ITO substrates and followed by a prebaking step at 120 °C for 60 s. The photoresist film was then exposed to UV light with 374 nm laser in the interference lithography setup for 2−3 min and developed in MF319 developer for 5 s. ITO and Ta:TiO_2 were then deposited by pulsed laser deposition (PLD). The substrate was soaked in acetone for 15 min to remove the templated photoresist followed by annealing at 400 °C for 15 min to enhance the Ta:TiO_2 conductivity.

Fabrication of PbS Solar Cells. PbS CQDs were deposited onto both patterned and planar ITO via dip-coating using a layer-by-layer (LBL) deposition technique in a nitrogen-filled glovebox (all fabrication steps in planar samples were identical to pattern devices, except for the lack of photolithography). The LBL technique consisted of the following deposition protocol. Substrates were dipped in four different solutions to deposit one layer of PbS film, namely (1) a mix ligand solution of 0.01% MPA and 0.01% BDT in acetonitrile as a linker solution, (2) 5 mg/mL PbS solution in hexane, (3) a mix ligand solution of 0.1% MPA and 0.1% BDT in acetonitrile as a exchange solution, and (4) acetonitrile as a rinsing solution. Substrates were soaked in each solution for 10 s and withdrawn at a speed of 1 mm/s followed by a drying time of 60 s. This cycle was repeated 50 or 90 times to obtain desired thickness of PbS films, which were 70−80 and 150−160 nm, respectively. The film-coating processes were performed using a fully automated dip-coating machine, and the withdraw speeds were selected to ensure uniform and conformal coating of the PbS nanocrystals unto the grating structures. To form a photocathode, 15 nm of MoO_3, 25 nm of Au, and then 120 nm of Ag were subsequently deposited in a thermal evaporator at a base pressure of 10^{-6} mbar. Devices were prepared and tested in a nitrogen-filled glovebox (O_2 < 0.1 ppm, H_2O < 0.1 ppm).

Characterization of PbS Solar Cells. *Absorption Measurement: CQD in Solution.* The absorption spectrum of PbS CQDs in octane was measured by UV−vis and NIR spectroscopy (Cary 60 UV−vis and NIR spectrophotometer) (Figure S1 in Supporting Information).

Absorption Measurement: Complete Solar Cells. The absorption of complete PbS solar cells was measured with an integrating sphere and spectrometer/CCD camera (Acton 300, PIXIS, Princeton Instruments).

Scanning Electron Microscopy. A scanning electron microscopy (FEI Helios 600 Nanolab Dual Beam System) was used to image the grating structures and determine the thickness of PbS films.

Current−Voltage Measurements. All the solar cell characterizations were employed in a nitrogen-filled glovebox. Current−voltage measurements were performed using a Keithley 2400 source meter. The photovoltaic characteristics of the solar cells were recorded under a simulated A.M. 1.5G (1000 W/m^2) solar illumination from a Newport solar simulator. Neutral density filters were used to vary the intensity of the incident light.

EQE Measurement. To measure the external quantum efficiency (EQE) of the devices, light originating from a halogen lamp was passed through a monochromator to produce a monochromatic light that was directly incident onto the solar cells resulting into a photocurrent, which was measured with a lock-in amplifier.

EIS Measurement. A Gamry 500 potentiostat with Gamry Framework was utilized to characterize the impedance of the photovoltaic devices.

RESULTS AND DISCUSSION

Role of Corrugated Structure on Photovoltaic Properties. Figure 1 shows the cross-sectional micrographs of the flat and grating devices. The PbS layer thickness was adjusted by the number of dip-coating cycles to be either ∼75 or ∼155 nm thick corresponding to 50 and 90 cycles, respectively. The grating geometry was achieved by first using laser interference lithography to pattern a photoresist onto which the ITO/Ta:TiO_2 layers were deposited by PLD. The ITO/Ta:TiO_2 grating was approximately 400 nm in height with a 600 nm period. These parameters were selected because of the facile

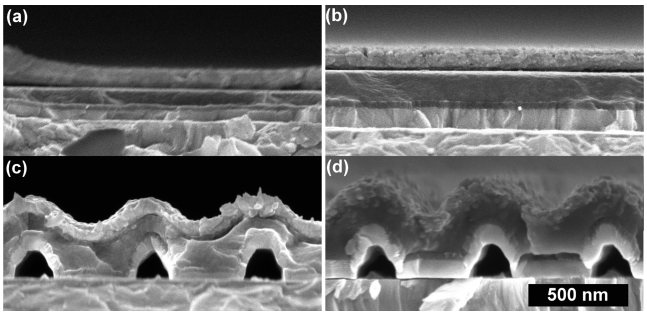

Figure 1. SEM images of flat and grating devices with 50 (a, c) or 90 (b, d) layers of PbS films.

fabrication, a step toward a truly optimized structure as modeled in reference which requires a larger structure height/pitch ratio.[21] As seen in Figures 1c and 1d, the grating devices maintain the corrugated structure of the patterned electrode without filling the space between the ridges by the subsequent layers.

The current density–voltage (J–V) characteristics and photovoltaic parameters of the flat and grating devices measured under 1 sun illumination are depicted in Figure 2a and Table 1, respectively. Six devices of each type were fabricated and tested for the data (Table 1). The performance figures were modest relative to champion devices published elsewhere. This is presumably because of more limited charge transport characteristics in our QDs, but nevertheless we noted clearly different metrics for the different device types. The detailed measurements presented below were taken for representative performers from the different groups. Increasing the PbS film thickness of the planar cells negatively impacted all measures of their performance with 46% decrease in overall energy conversion efficiency. Most significantly, the V_{oc} and FF decreased by 29% and 21%, respectively. Decreasing FF with increasing PbS film thickness for planar devices was predicted in simulations,[21] resulting from increased recombination of carriers photogenerated outside the depletion region. We note that this large drop in FF with PbS layer thickness was not seen with the grating structure, and this is partially also consistent with predictions.[21] Similarly, increasing PbS film thickness has resulted in a particularly severe reduction of V_{oc} in the flat samples. Though the source of the drop in V_{oc} as function PbS thickness can also be associated with carrier recombination factors, the role of the device architecture is not so simple to interpret.

For the remainder of the paper we discuss the role of grating on photovoltaic properties exclusively in devices comprising 50 layers of PbS (hereafter denoted as 50L), whose thickness is 70–80 nm. Overall, the grating structure improved the power conversion efficiency by 20% over the planar geometry.

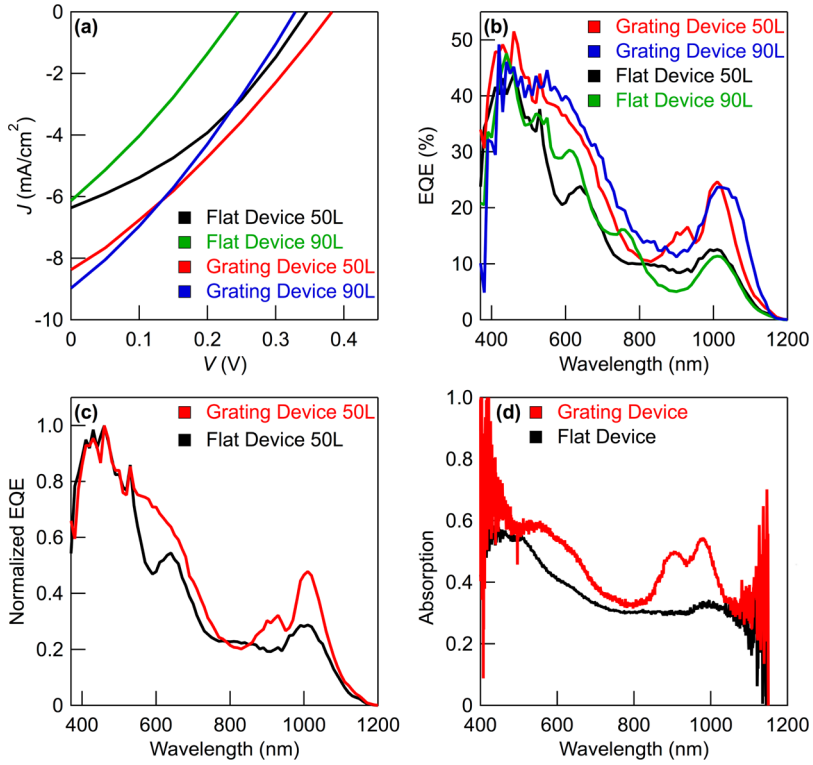

Figure 2. (a) Current–voltage characteristics of the flat and grating solar cells with two different PbS thicknesses, (b) the external quantum efficiency (EQE) of the four solar cells, (c) normalized EQE of 50 layers PbS flat and grating devices, and (d) absorption spectra of devices with 50 layers of PbS in the flat and grating architectures.

Table 1. Photovoltaic Parameters of the Solar Cells Measured under A.M. 1.5 1 sun Illumination

device type	PbS thickness (nm)	J_{sc} (mA/cm^2)	V_{oc} (V)	FF (%)	efficiency (%)
flat 50L	70–80	6.36 ± 0.22	0.35 ± 0.07	35.68 ± 6.40	0.79 ± 0.40
flat 90L	150–160	6.14 ± 0.42	0.25 ± 0.02	28.31 ± 1.87	0.43 ± 0.12
grating 50L	70–80	8.37 ± 0.55	0.38 ± 0.06	29.47 ± 2.06	0.95 ± 0.31
grating 90L	150–160	8.97 ± 0.87	0.33 ± 0.03	29.66 ± 1.46	0.87 ± 0.17

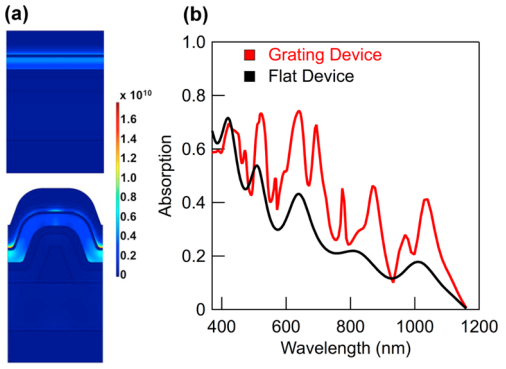

Figure 3. (a) Simulated optical absorption in the flat (top) and grating (bottom) solar cells and (b) simulated absorption spectra of the PbS flat and grating devices.

Given that the grating increases the volume of PbS per projected 2-dimensional area without affecting the charge collection dynamics, much of the 32% enhancement in J_{sc} is attributed to increased charged generation in the extra volume. In addition, simulations (Figure 3) predict the charge generation rate in the grating device to be enhanced by light-field localization, which is consistent measured absorption spectra of Figure 2d, whereas in the simulation, enhanced absorption occurs for wavelengths greater than 550 nm, especially near the PbS CQD's excitonic 800−1100 nm peak range. This enhanced light absorption over these wavelengths for the grating device is mirrored in the external quantum efficiency (EQE) spectra displayed in Figure 2c,d. Notably, a 2-fold enhancement in EQE was achieved for the PbS CQD's excitonic peak centered at 1000 nm in the devices structured by the interference lithography step.

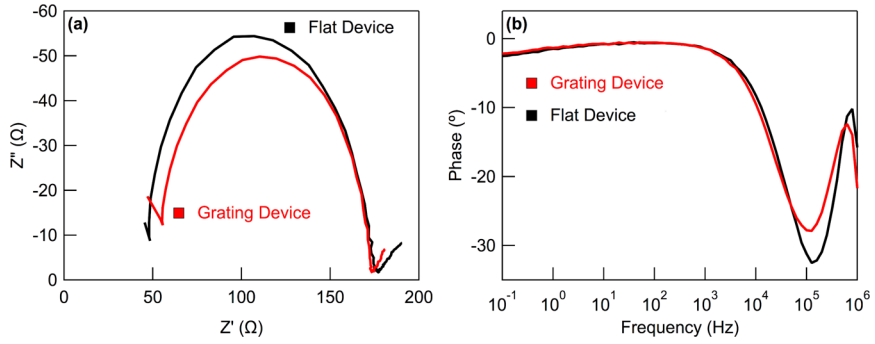

Figure 4. (a) Nyquist plot and (b) Bode plot of 50L flat and grating solar cells.

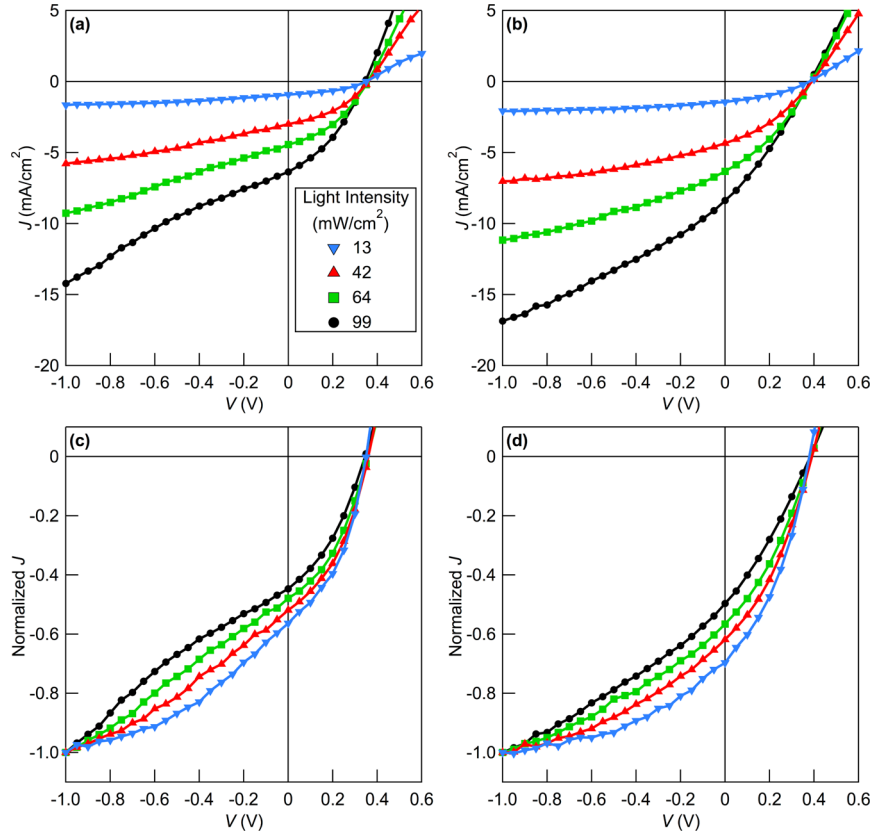

Figure 5. Current−voltage characteristics of (a) the flat and (b) grating solar cells as a function of light intensity. (c, d) Charge collection probabilities of the devices, which were calculated by normalizing the photocurrent measured at the various light intensities with the saturated photocurrent measured at −1 V, respectively.

Losses Analysis Based on White Light Intensity-Dependent Measurements. In order to better investigate the origin of the differences in device electrical parameters, we have evaluated the interfacial and bulk properties using electrical impedance spectroscopy (EIS). The Nyquist plot (Figure 4a) for the patterned and flat devices shows that the grating device has a slightly lower internal resistance compared to the flat device, whereas the sheet resistance for the grating device was higher probably due to the imperfect interfacial contact between the commercial ITO and PLD deposited ITO. On the other hand, referring to the Bode plot shown in Figure 4b, we observed that the impedance phase peaks at similar frequencies for both type of devices. These frequencies correspond to the rate constant for the recombination of injected electrons in the semiconducting film, which is inversely proportional to electron lifetime.[24] These EIS results suggest that the electron recombination rate at V_{oc} for both device types must be very similar, thus eliminating a possible enhanced recombination as the source of the notable FF and V_{oc} difference between the nanostructured and planar cells.

In order to uncover the source of the devices performance contrast, we further investigated the charge recombination processes in more detail by studying light-intensity dependent photovoltaic $J-V$ characteristics. By analyzing the charge collection probability of the devices as a function of light intensity, the voltage range over which bimolecular or monomolecular recombination occurs can be determined. In a simplified model, the photocurrent of the cells comprising a PbS film of thickness d is expressed as $J_{ph} = q\int G(\mathrm{LI})\, dz\, P_c(\mathrm{LI},V)$,[25] where $G(\mathrm{LI})$ is the photon flux absorbed by the solar cell per unit volume and $P_c(\mathrm{LI},V)$ is the charge collection probability (G is clearly a function of the light intensity (LI) and P_c could possibly be). This probability can be expressed in a more general way independent of the device geometry as $P_c(\mathrm{LI},V) = |J_{ph}(\mathrm{LI},V)/(J_{ph}$ at saturation)|.[25] Approximating the current saturation point to be at −1 V for both flat and grating devices, $q\int G(\mathrm{LI})\, dz = J_{ph}(V = -1\ \mathrm{V})$, the collection probability is then simply expressed as $P_c(\mathrm{LI},V) = |J_{ph}(\mathrm{LI},V)/J_{ph}(\mathrm{LI}, -1\ \mathrm{V})|$. Figure 5 shows the photovoltaic performance of the solar cells recorded under various light intensities ((a) flat and (b) grating) and the charge collection probabilities of the devices, which were calculated by the approximation outlined above (Figure 5c,d). We note that collection probabilities at difference light intensities do not overlap. This is a strong indication of the dominance of bimolecular recombination[25] for both device types, although the shape of the curves are significantly distinct. In the flat cell, the dispersion of the normalized curves is relatively small in the positive applied bias, increasing significantly for the reverse bias region (Figure 5c). For the patterned cell, the all the curves seem to be fairly dispersed at all applied voltage biases (Figure 5d).

Focusing on the $J-V$ curves collected under the highest and lowest light intensities (Figure 6a), it is clear that the flat device was more severely affected by light intensity under the voltage range of −0.8 to −0.2 V, whereas the grating device was more affected under the voltage range of −0.2 to near V_{oc} compared to the flat device. Figure 6b shows a more detailed analysis of loss processes by analyzing the power exponent, α, in the relationship of $J_{ph} \propto (\mathrm{LI})^{\alpha}$, where J_{ph} is the photogenerated current density (the difference between the total current measured under light illumination and the dark current), and as above LI is the incident light intensity.[25−27] In this expression, α quantifies the linearity of their relationship: α becomes unity

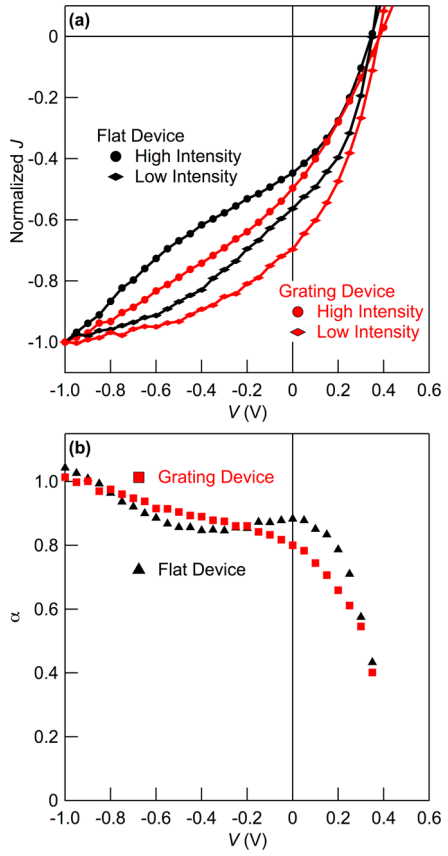

Figure 6. (a) $J-V$ curves collected under highest and lowest light intensity of the flat (dark color) and grating (red color) devices and (b) the proportionality factor α relating current density to light intensity ($J_{ph} \propto$ (light intensity)$^{\alpha}$).

when all charges are collected without loss whereas sublinear values may result from a carrier mobility imbalance, space charges, or bimolecular recombination. As observed, α turns out to be sublinear for both device types (Figure 6b), but also it is evident that lower values of α were measured for the flat device over the voltage range of −0.8 to −0.2 V, while for applied voltages exceeding −0.2 V, lower α values were calculated for the grating device. The result indicates that bimolecular recombination is occurring to a greater extent in the grating device, especially in the range of the cell's working voltage range (from 0 voltage to V_{oc}) most likely accounting for part of the reduction in FF for the grating devices compared to flat devices (Figure 3a and Table 1), 29.47% and 35.68%, respectively.

Losses Analysis Based on Monochromatic Light Intensity-Dependent Measurements. It is not obvious why the two types of devices would show such significant difference in bimolecular recombination at different biases. In order to understand the source of the difference, we have analyzed light intensity dependent photocurrent measurements under three different light sources reaching current densities comparable to those of the white light A.M. 1.5 solar simulator, namely a blue laser (λ = 473 nm), a red laser (λ = 633 nm), and a white light source with an IR long-pass filter (hereafter denoted as $\lambda \geqslant 700$ nm). Figure 7 shows the $J-V$ curves measured while the devices were exposed to those selected light sources. One can observe that, in contrast to the while light experiment, the $J-V$ curves are all qualitatively smoother and monotonic at all applied voltages. We noted to that a very

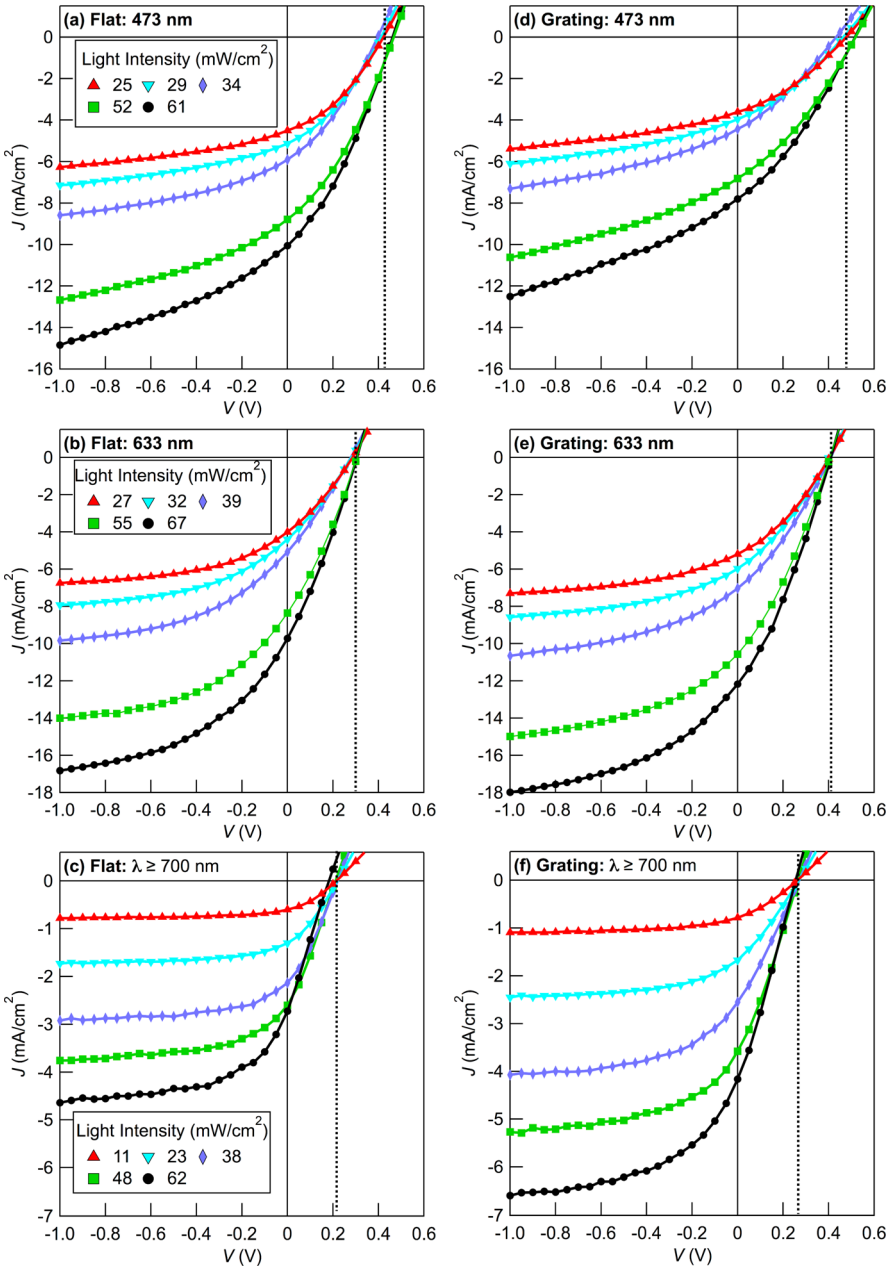

Figure 7. Current–voltage characteristics of flat and grating devices collected over the wavelength of (a, d) 473 nm, (b, e) 633 nm, and (c, f) $\lambda \geqslant 700$ nm.

distinct maximum V_{oc} is obtained as a function of wavelength. In order to elucidate the dominating loss processes under wavelength controlled illumination, we have analyzed the charge collection probabilities by studying the nature of the normalized current–voltage curves under different light intensities for all device types (Figure 8). Very remarkably, varying the intensity of the three different light sources has a modest effect on the shape of the normalized J–V curves. In particular, the curves corresponding to $\lambda = 633$ nm and $\lambda \geq 700$ nm in the grating devices overlap extremely well, indicating that the current loss due to the bimolecular recombination was minimal for these wavelengths. It should be mentioned that this explains (beyond the pattern enhanced light absorption) the 2-fold EQE enhancement around $\lambda = 1000$ nm of the grating device relative the flat counterpart (Figure 3b). More IR light is indeed absorbed by the pattern, but it is also collected more efficiency than at shorter wavelengths. For both flat and grating devices, higher EQEs were recorded at wavelengths of 473 and 633 nm compared to the value measured at $\lambda \geqslant 700$ nm (Figure 3b); the result from Figure 8 shows this is a result of the larger optical absorption only as this occurs in fact under a higher probability for bimolecular recombination.

By making a close analysis of the curves measured under the three different light sources, we observed that the values of V_{oc} were wavelength-dependent rather than a function of the light intensity. In general, it is expected V_{oc} will depend on the light intensity via the connection between LI and J_{ph} and the ideal diode equation $V_{oc} = n(kT/q)\ \ln(J_{ph}/J_0 + 1)$,[28–30] where J_0, q, n, k, and T represent the reverse saturation current density, elementary charge, diode ideality factor, Boltzmann constant, and absolute temperature, respectively. As seen in Figure 7, the values of V_{oc} for both the flat and grating devices

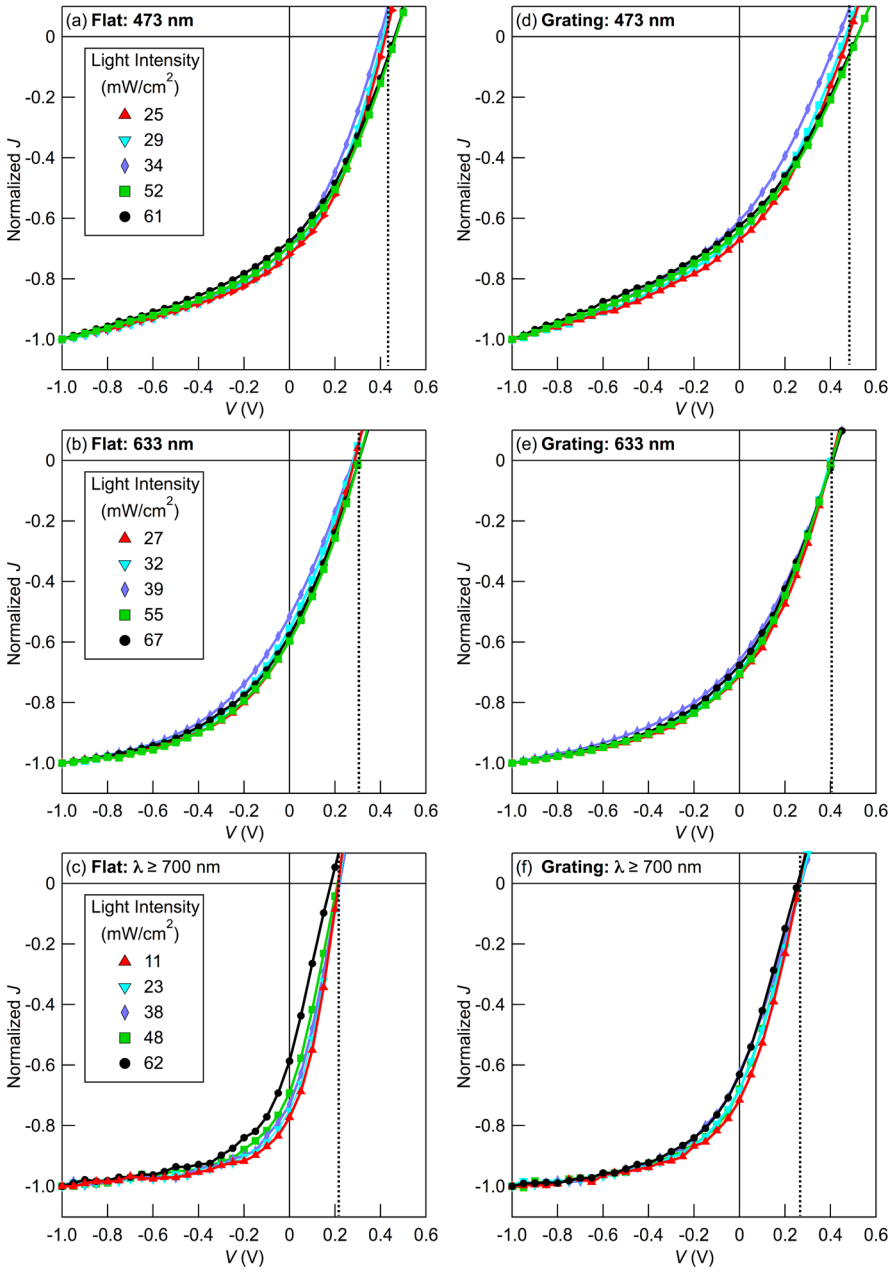

Figure 8. Charge collection probabilities of the devices collected over the wavelength of (a, d) 473 nm, (b, e) 633 nm, and (c, f) $\lambda \geqslant 700$ nm, which were calculated by normalizing the photocurrent measured at the various light intensities with the saturated photocurrent measured at −1 V.

did not change as a function of light intensity; this is because given the ideal diode logarithmic relationship, V_{oc}, will only vary significantly upon light intensity variations that span orders of magnitude. Nonetheless, the V_{oc} values become lower with larger light wavelengths (decreasing photon energy) for both device types (see the dotted line in Figures 7 and 8). Figure 9 shows the V_{oc} values from Figure 7 as a function of photon flux in order to consider the number of photons rather than merely light intensity and make a fair comparison across illumination sources. Although the V_{oc} measured under 473 nm light irradiation show a modest dependency of photon flux for both devices, the V_{oc} were nearly constant regardless of the photon flux. However, the V_{oc} decreased dramatically with the longer wavelengths. To the best of our knowledge, there have been no reports about V_{oc} depending upon wavelength in quantum dot-based solar cells.

The strict dependence of V_{oc} on wavelength for a given incident light flux is an interesting phenomenon that has a direct link with the material's intrinsic properties. The V_{oc} of the solar cells is determined by the electron and hole quasi-Fermi levels, which in turn are controlled by the photogenerated charges accumulated in the density of states (DOS).[31,32] In other words, the charge density residing in the DOS is the limiting factor for V_{oc}. Since PbS nanoparticles are well-known to have localized charge traps, it can safely be imagined that carriers created by different light energies have different distribution in the DOS. It is well understood that trapped charges in PbS quantum dots leads to Fermi energy pinning which directly affects the measured photovoltage in solar cells.[33] PbS sub-bandgap states are also known to give rise to radiative recombination processes which also reduces open-circuit voltage.[34,35] The signature of sub-bandgaps states is also evident

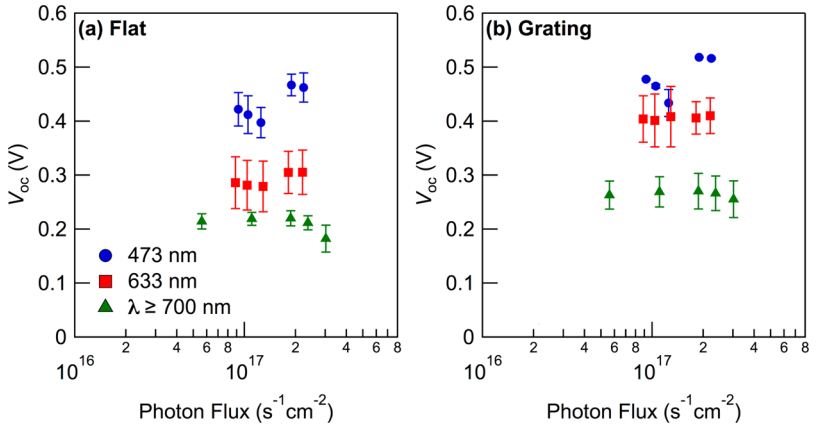

Figure 9. V_{oc} as a function of photon flux with different light sources for (a) flat and (b) grating devices.

in photoinduced absorption experiments.[36] The fact that the open-circuit voltage increases with the excitation photon energy may indicate that carriers generated by the low-energy photons are more susceptible to trapping in sub-bandgap states while most of the charge carriers generated by the high-energy photons are effectively swept out. Thus, blue photon-generated charges occupy higher levels of DOS, thereby widening the gap of the electron and hole Fermi energy levels (larger V_{oc}), whereas charges created by low-energy photons (red−NIR) can easily be trapped in the tail of the DOS or sub-bandgap states and resulting into low V_{oc}. This observation is extremely important in understanding the commonly low V_{oc} of PbS quantum dot solar cells regardless of material bandgap[14] and power conversion efficiency.

The above-noted observations help greatly to explain the differences between the flat and grating devices. Although delivering similar efficiencies and appearing nearly identical under EIS measurements, the patterned and planar devices show differences in FF and V_{oc} due to their different wavelength-weighted responses. The most distinct electrical benefit of nanostructuring was found for carriers generated by near-infrared photons, with larger harvesting probabilities and larger V_{oc}'s when probed under IR light only. This suggests the grating structure not only provides enhanced light absorption, but it lowers the transport losses for the low-energy-generated carriers. An optimized grating structure could then be utilized to amplify the infrared light-generated photocurrent yield of all CQD devices. Further investigation is needed to enhance the charge collection efficiency of the grating devices while optimizations are also necessary to achieve even better optical absorption and distributions within the active CQD films. It is also quite interesting to recognize a wavelength-dependent V_{oc}, which is an indicative of varying special distribution of charge carriers in DOS depending on what photon energy was absorbed to create carriers: charges created by low-energy photons are more likely localized in the tail of the DOS, thereby lowering Fermi energy levels and hence lower V_{oc}. Under white light illumination, the different quasi-Fermi levels splitting achieved by different wavelengths are convoluted in an overall $J-V$ curve that mixes DOS structure and photonic/transport properties.

CONCLUSIONS

In summary, we have shown that the performance of PbS solar cells was improved by utilizing an electrode with a grating structure. Compared to flat device, a 32% higher J_{sc} was achieved from the grating device. Although the grating device suffered due to higher bimolecular recombination, its light confinement property is quite appealing. Furthermore, despite its lower FF due to the recombination and V_{oc}−wavelength dependence, the power conversion efficiency of the grating device was 20% higher than that of flat counterpart resulting from the higher current generation. The V_{oc}−wavelength dependence for PbS solar cells has been identified and can be used to understand $J-V$ curves under full white light illumination. Clear experimental evidence was presented showing an increase of transport length or reduced bimolecular losses for carriers generated by absorption of near-infrared photons. These results show a picture of the interaction of the device architecture with the materials properties to give rise to distinct photovoltaic performances. Nanofabrication advances are required to realize this and more sophisticated architectures in robust and easy way in order to effectively be able to remedy some materials shortcomings via device geometrical design.

ASSOCIATED CONTENT

Supporting Information

The Supporting Information is available free of charge on the ACS Publications website at DOI: 10.1021/acs.jpcc.6b01498.

Figure S1 (PDF)

AUTHOR INFORMATION

Corresponding Author

*E-mail hara@ad.unc.edu; phone 608-698-0486 (Y.H.).

Present Address

A.G.: Department of Physics and ORaCEL, North Carolina State University, Raleigh, North Carolina 27695, USA.

Notes

The authors declare no competing financial interest.

ACKNOWLEDGMENTS

This material is based upon work funded by the U.S. Department of Energy, Office of Science, and Office of Basic Energy Sciences under Award DE-SC0006416. We also acknowledge support by Research Corporation for the Science Advancement #22371. The authors also thank Chapel Hill Analytical and Nanofabrication Laboratory (CHANL) for all their assistance.

REFERENCES

(1) Luther, J. M.; Law, M.; Beard, M. C.; Song, Q.; Reese, M. O.; Ellingson, R. J.; Nozik, A. J. Schottky Solar Cells Based on Colloidal Nanocrystal Films. *Nano Lett.* **2008**, *8*, 3488−3492.

(2) Tang, J.; Sargent, E. H. Infrared Colloidal Quantum Dots for Photovoltaics: Fundamentals and Recent Progress. *Adv. Mater.* **2011**, *23*, 12−29.

(3) Ip, A. H.; Thon, S. M.; Hoogland, S.; Voznyy, O.; Zhitomirsky, D.; Debnath, R.; Levina, L.; Rollny, L. R.; Carey, G. H.; Fischer, A.; et al. Hybrid Passivated Colloidal Quantum Dot Solids. *Nat. Nanotechnol.* **2012**, *7*, 577−582.

(4) Chuang, C.-H. M.; Brown, P. R.; Bulović, V.; Bawendi, M. G. Improved Performance and Stability in Quantum Dot Solar Cells through Band Alignment Engineering. *Nat. Mater.* **2014**, *13*, 796−801.

(5) Steckel, J. S.; Coe-Sullivan, S.; Bulović, V.; Bawendi, M. G. 1.3 to 1.55 μm Tunable Electroluminescence from PbSe Quantum Dots Embedded within an Organic Device. *Adv. Mater.* **2003**, *15*, 1862−1866.

(6) Konstantatos, G.; Huang, C.; Levina, L.; Lu, Z.; Sargent, E. H. Efficient Infrared Electroluminescent Devices Using Solution-Processed Colloidal Quantum Dots. *Adv. Funct. Mater.* **2005**, *15*, 1865−1869.

(7) Sun, L.; Choi, J. J.; Stachnik, D.; Bartnik, A. C.; Hyun, B.-R.; Malliaras, G. G.; Hanrath, T.; Wise, F. W. Bright Infrared Quantum-Dot Light-Emitting Diodes through Inter-Dot Spacing Control. *Nat. Nanotechnol.* **2012**, *7*, 369−373.

(8) Konstantatos, G.; Howard, I.; Fischer, A.; Hoogland, S.; Clifford, J.; Klem, E.; Levina, L.; Sargent, E. H. Ultrasensitive Solution-Cast Quantum Dot Photodetectors. *Nature* **2006**, *442*, 180−183.

(9) Zhang, C.-Y.; Yeh, H.-C.; Kuroki, M. T.; Wang, T.-H. Single-Quantum-Dot-Based DNA Nanosensor. *Nat. Mater.* **2005**, *4*, 826−831.

(10) Cunningham, P. D.; Boercker, J. E.; Foos, E. E.; Lumb, M. P.; Smith, A. R.; Tischler, J. G.; Melinger, J. S. Enhanced Multiple Exciton Generation in Quasi-One-Dimensional Semiconductors. *Nano Lett.* **2011**, *11*, 3476−3481.

(11) Semonin, O. E.; Luther, J. M.; Choi, S.; Chen, H.-Y.; Gao, J.; Nozik, A. J.; Beard, M. C. Peak External Photocurrent Quantum Efficiency Exceeding 100% via MEG in a Quantum Dot Solar Cell. *Science* **2011**, *334*, 1530−1533.

(12) Gao, J.; Luther, J. M.; Semonin, O. E.; Ellingson, R. J.; Nozik, A. J.; Beard, M. C. Quantum Dot Size Dependent J-V Characteristics in Heterojunction ZnO/PbS Quantum Dot Solar Cells. *Nano Lett.* **2011**, *11*, 1002−1008.

(13) Lan, X.; Masala, S.; Sargent, E. H. Charge-Extraction Strategies for Colloidal Quantum Dot Photovoltaics. *Nat. Mater.* **2014**, *13*, 233−240.

(14) Brown, P. R.; Kim, D.; Lunt, R. R.; Zhao, N.; Bawendi, M. G.; Grossman, J. C.; Bulović, V. Energy Level Modification in Lead Sulfide Quantum Dot Thin Films through Ligand Exchange. *ACS Nano* **2014**, *8*, 5863−5872.

(15) Rath, A. K.; Bernechea, M.; Martinez, L.; de Arquer, F. P. G.; Osmond, J.; Konstantatos, G. Solution-Processed Inorganic Bulk Nano-Heterojunctions and Their Application to Solar Cells. *Nat. Photonics* **2012**, *6*, 529−534.

(16) Zhitomirsky, D.; Voznyy, O.; Levina, L.; Hoogland, S.; Kemp, K. W.; Ip, A. H.; Thon, S. M.; Sargent, E. H. Engineering Colloidal Quantum Dot Solids within and beyond the Mobility-Invariant Regime. *Nat. Commun.* **2014**, *5*, 3803.

(17) Park, H.; Chang, S.; Jean, J.; Cheng, J. J.; Araujo, P. T.; Wang, M.; Bawendi, M. G.; Dresselhaus, M. S.; Bulović, V.; Kong, J.; et al. Graphene Cathode-Based ZnO Nanowire Hybrid Solar Cells. *Nano Lett.* **2013**, *13*, 233−239.

(18) Wang, H.; Kubo, T.; Nakazaki, J.; Kinoshita, T.; Segawa, H. PbS-Quantum-Dot-Based Heterojunction Solar Cells Utilizing ZnO Nanowires for High External Quantum Efficiency in the near-Infrared Region. *J. Phys. Chem. Lett.* **2013**, *4*, 2455−2460.

(19) Kramer, I. J.; Zhitomirsky, D.; Bass, J. D.; Rice, P. M.; Topuria, T.; Krupp, L.; Thon, S. M.; Ip, A. H.; Debnath, R.; Kim, H. C.; et al. Ordered Nanopillar Structured Electrodes for Depleted Bulk Heterojunction Colloidal Quantum Dot Solar Cells. *Adv. Mater.* **2012**, *24*, 2315−2319.

(20) Labelle, A. J.; Thon, S. M.; Masala, S.; Adachi, M. M.; Dong, H.; Farahani, M.; Ip, A. H.; Fratalocchi, A.; Sargent, E. H. Colloidal Quantum Dot Solar Cells Exploiting Hierarchical Structuring. *Nano Lett.* **2015**, *15*, 1101−1108.

(21) Fu, Y.; Dinku, A. G.; Hara, Y.; Miller, C. W.; Vrouwenvelder, K. T.; Lopez, R. Modeling Photovoltaic Performance in Periodic Patterned Colloidal Quantum Dot Solar Cells. *Opt. Express* **2015**, *23*, A779−A790.

(22) Hines, M. A.; Scholes, G. D. Colloidal PbS Nanocrystals with Size-Tunable Near-Infrared Emission: Observation of Post-Synthesis Self-Narrowing of the Particle Size Distribution. *Adv. Mater.* **2003**, *15*, 1844−1849.

(23) Noone, K. M.; Strein, E.; Anderson, N. C.; Wu, P. T.; Jenekhe, S. A.; Ginger, D. S. Broadband Absorbing Bulk Heterojunction Photovoltaics Using Low-Bandgap Solution-Processed Quantum Dots. *Nano Lett.* **2010**, *10*, 2635−2639.

(24) Adachi, M.; Sakamoto, M.; Jiu, J. T.; Ogata, Y.; Isoda, S. Determination of Parameters of Electron Transport in Dye-Sensitized Solar Cells Using Electrochemical Impedance Spectroscopy. *J. Phys. Chem. B* **2006**, *110*, 13872−13880.

(25) Cowan, S. R.; Roy, A.; Heeger, A. J. Recombination in Polymer-Fullerene Bulk Heterojunction Solar Cells. *Phys. Rev. B: Condens. Matter Mater. Phys.* **2010**, *82*, 245207.

(26) Cowan, S. R.; Banerji, N.; Leong, W. L.; Heeger, A. J. Charge Formation, Recombination, and Sweep-out Dynamics in Organic Solar Cells. *Adv. Funct. Mater.* **2012**, *22*, 1116−1128.

(27) Proctor, C. M.; Kim, C.; Neher, D.; Nguyen, T. Q. Nongeminate Recombination and Charge Transport Limitations in Diketopyrrolopyrrole-Based Solution-Processed Small Molecule Solar Cells. *Adv. Funct. Mater.* **2013**, *23*, 3584−3594.

(28) Koster, L. J. A.; Mihailetchi, V. D.; Ramaker, R.; Blom, P. W. M. Light Intensity Dependence of Open-Circuit Voltage of Polymer:-fullerene Solar Cells. *Appl. Phys. Lett.* **2005**, *86*, 123509.

(29) Vandewal, K.; Tvingstedt, K.; Gadisa, A.; Inganäs, O.; Manca, J. V. On the Origin of the Open-Circuit Voltage of Polymer-Fullerene Solar Cells. *Nat. Mater.* **2009**, *8*, 904−909.

(30) Wetzelaer, G. a H.; Kuik, M.; Lenes, M.; Blom, P. W. M. Origin of the Dark-Current Ideality Factor in Polymer:fullerene Bulk Heterojunction Solar Cells. *Appl. Phys. Lett.* **2011**, *99*, 153506.

(31) Garcia-Belmonte, G.; Boix, P. P.; Bisquert, J.; Lenes, M.; Bolink, H. J.; La Rosa, A.; Filippone, S.; Martín, N. Influence of the Intermediate Density-of-States Occupancy on Open-Circuit Voltage of Bulk Heterojunction Solar Cells with Different Fullerene Acceptors. *J. Phys. Chem. Lett.* **2010**, *1*, 2566−2571.

(32) Shao, Y.; Yuan, Y.; Huang, J. Correlation of Energy Disorder and Open-Circuit Voltage in Hybrid Perovskite Solar Cells. *Nat. Energy* **2016**, *1*, 15001.

(33) Bozyigit, D.; Lin, W. M. M.; Yazdani, N.; Yarema, O.; Wood, V. A Quantitative Model for Charge Carrier Transport, Trapping and Recombination in Nanocrystal-Based Solar Cells. *Nat. Commun.* **2015**, *6*, 6180.

(34) Chuang, C. H. M.; Maurano, A.; Brandt, R. E.; Hwang, G. W.; Jean, J.; Buonassisi, T.; Bulović, V.; Bawendi, M. G. Open-Circuit Voltage Deficit, Radiative Sub-Bandgap States, and Prospects in Quantum Dot Solar Cells. *Nano Lett.* **2015**, *15*, 3286−3294.

(35) Kim, D.; Kuwabara, T.; Nakayama, M. Photoluminescence Properties Related to Localized States in Colloidal PbS Quantum Dots. *J. Lumin.* **2006**, *119−120*, 214−218.

(36) Zhang, J.; Jiang, X. Confinement-Dependent below-Gap State in PbS Quantum Dot Films Probed by Continuous-Wave Photoinduced Absorption. *J. Phys. Chem. B* **2008**, *112*, 9557−9560.